Deep mantle origin of large igneous provinces and komatiites

Rémy Pierru, Denis Andrault, Geeth Manthilake, Julien Monteux, Jean-Luc Devidal, Nicolas Guignot, Andrew King, Laura Henry

▶ To cite this version:

Rémy Pierru, Denis Andrault, Geeth Manthilake, Julien Monteux, Jean-Luc Devidal, et al.. Deep mantle origin of large igneous provinces and komatiites. Science Advances , 2022, 8 (44), 10.1126/sciadv.abo1036 . hal-03850999

HAL Id: hal-03850999

https://uca.hal.science/hal-03850999v1

Submitted on 14 Nov 2022

PLANETARY SCIENCE

Deep mantle origin of large igneous provinces and komatiites

Rémy Pierru[1]*, Denis Andrault[1], Geeth Manthilake[1], Julien Monteux[1], Jean Luc Devidal[1], Nicolas Guignot[2], Andrew King[2], Laura Henry[2]

Large igneous provinces (LIPs) resulted from intraplate magmatic events mobilizing volumes of magma up to several million cubic kilometers. LIPs and lavas with deep mantle sources have compositions ranging from komatiites found in Archean greenstone belts to basalts and picrites in Phanerozoic flood basalt and recent oceanic islands. In this study, we identify the mantle conditions appropriate to each type of lava based on an experimental study of the melting of pyrolite. The depth of the mantle source decreases from 600 to 700 km for the oldest komatiites to 100 to 300 km for picrites and basalts, and the extent of mantle melting ranges from 10 to 50%. We develop a geodynamical model that explains the origin of the hot mantle plumes capable of generating these melting *P-T* conditions. Within a superadiabatic temperature gradient persisting in the deep mantle, the ascent of hot mantle plumes creates excess temperatures up to 250 to 300 K by adiabatic decompression.

INTRODUCTION

The mantle potential temperature

The mantle temperature (T) is generally defined by the potential surface temperature (T_p), which corresponds to the extrapolation to the surface of the adiabatic T gradient. The mantle T_p can be refined from the analysis of primary magmas formed along accretionary ridges (*1*) and is calculated after a calibration of, e.g., the melt MgO content against several parameters including T and pressure (P) (*2*, *3*). Currently, T_p of 1350° ± 50°C is suggested by primary basalts with MgO and FeO contents at 10 to 13 weight % (wt%) and 6.5 to 8.0 wt%, respectively (*4*). Still, there are "hot" primary magmas (basaltic-picritic) requiring T_p as high as ~1600°C (*5*). These are "hot spots," such as Hawaii, and they could be related to instabilities in the thermal boundary layer in the lowermost mantle (*6*).

The Archean mantle T_p has important implications for understanding the geodynamics of the early Earth and the onset of plate tectonics. Recent geodynamic models have recognized the importance of the reevaluation of Archean mantle T_p for crustal formation mechanisms in stagnant lava environments (*7*). Average T_p estimates for large igneous provinces (LIPs) and Hawaii is $\Delta T = +200$ K or higher than the average mantle T_p. In Tortugal, where komatiites occur, ΔT can exceed +300 K (*8*).

Regarding the accuracy of the T_p determination, note that the agreement between the compositions of experimental melts and primary magmas on the field are in very good agreement only if the source is not very deep (P lower than 6 to 7 GPa). At higher P, the accuracy of T_p is more questionable, especially for Archean sources of ultramafic rocks. This is, in part, because experimental conditions are less well controlled at high P and the composition of the melt at equilibrium is also more difficult to measure. For example, estimates of the T_p required to produce a primary magma with MgO >20 wt% diverge by ~100 K with the PRIMELT calculation (*3*). In a more general manner, any uncertainty on the melting diagram is directly transferred into uncertainties on the knowledge of the melting condition in the mantle.

In addition to this, anomalously high water contents in the mantle could produce comparable effects as high T, as water lowers the solidus. Where T_p estimates from dry material show rather consistent results, melts produced from a wet mantle do not seem to provide usable computational solutions (*9*). More generally, the likely presence of chemical heterogeneities increases the uncertainty on the T_p determination locally (*10*).

A broad range of primitive lavas

Mafic-ultramafic tholeiitic lavas such as basalts, picrites, and komatiites (*11*) represent the deepest and hottest magmas that erupted on Earth. Three main families of komatiites are distinguished depending on their chemical composition; nicknames have been given to them according to locality of the main outcrops (*12*): Al-depleted komatiites (ADK; Barberton type), Al-undepleted komatiites (AUK; Munro type), and Al-enriched komatiites/picrites (AEK; Gorgona type). These rocks show a large diversity of chemical composition resulting from different geological contexts including (i) mantle source, composition, depth, extent of melting (Φ), and possible presence of fluids and (ii) fractional crystallization, contamination, or assimilation possibly occurring during the ascent of melts to the lithosphere (*13*). There is a clear evolution of the composition of LIPs and komatiites through time over the past ~4 billion years (Ga; Fig. 1 and fig. S1). Unlike basalts and picrites that can be found at all ages, ADK seems to be only formed during the Archean from −4 to −2.8 Ga, while AUK erupted until about −1.9 Ga in Paleo-Proterozoic. Association of basalts and picrites with komatiites can be found, for example, in the form of dykes into Archean greenstone belts (*14*). Last, AEK formed from the Archean to the Phanerozoic. The most recent komatiites have been dated at ~90 Ma (*15*).

Picrites are rare intrusive igneous lavas enriched in magnesium (>12% MgO) (*16*) compared to the basalts erupting today on Earth. These lavas seem to be products of mantle melting at P above ~3 GPa and extent of melting (Φ) close to 20 to 30% (*17*). However, several other possible origins were proposed such as high rate of melting of lherzolitic mantle, partial melting of mantle with high Mg content, or olivine enrichment through processes of magmatic differentiation.

---

[1]Université Clermont Auvergne, CNRS, IRD, OPGC, LMV, F-63000 Clermont-Ferrand, France. [2]Synchrotron SOLEIL, Gif-sur-Yvette, France.
*Corresponding author. Email: r.pierru30@gmail.com

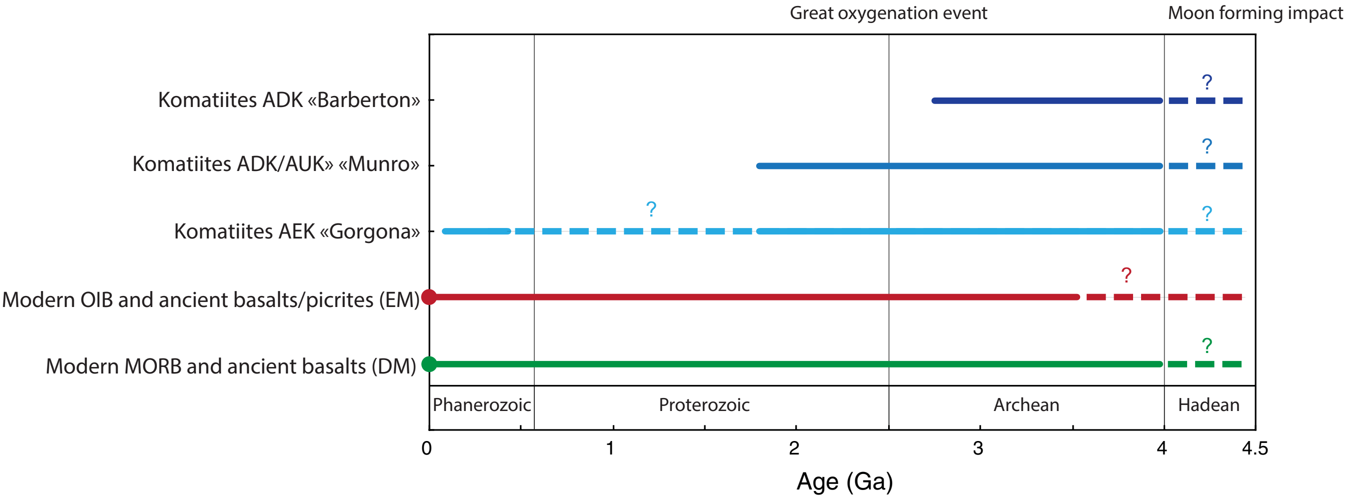

Fig. 1. Age of the different lavas found in LIPs: References are the same as those used for fig. S1.

Komatiites contain up to 34 wt% MgO, present very high liquidus *T* at atmospheric *P* (*18*) and have a close chemical relationship with mantle peridotites. For these reasons, komatiites must have formed at relatively high extents of melting in a mantle warmer than today (+200 to 300 K) (*1*). Alternatively, komatiites could be hydrated magmas formed at *T* not much higher than the surrounding mantle (*5*); the source of volatiles would be non-degassed primordial mantle or subducted oceanic crust.

1) ADKs present the very high MgO contents (≥30 wt%) and CaO/Al_2O_3 ratios (>~1.5), low $A1_20_3/TiO_2$ ratios (<10 to 15), and high Gd/Yb ratios, compared to chondrites. They are also enriched in trace elements and light rare earth elements (REEs) but depleted in heavy REE (HREE). However, their composition could not be reproduced experimentally from melting of typical mantle materials. Still, we note that CaO/Al_2O_3 ratios greater than 1.5 in melts were successfully reproduced by melting either KLB-1 peridotite at extent lower than 1% (*19*), peridotite with addition of up to 10% water (*20*), or ad hoc dry or hydrated $CaO\text{-}MgO\text{-}Al_2O_3\text{-}SiO_2$ (CMAS) compositions (*21*). The composition of ADK suggests melting with a residual Al-bearing phase (majoritic garnet and bridgmanite), which requires *P* over 15 to 17 GPa (*22*–*25*). Zirconium and hafnium, which are high in ADK, act as incompatible elements for melting processes at moderate Φ only (*26*), suggesting ADK magmas produced at lower Φ (~30%) than the other Archean komatiites.

2) AUKs present low $CaO/A1_2O_3$ ratios (~1 or less), high Al_20_3/TiO_2 ratios (~15 to 20), low MgO content (<30 wt%) compared to ADK, and an REE pattern close to chondrites. A robust characteristic is moderate to strong depletion of HREE and other immobile incompatible trace elements. The degree of depletion approaches, but rarely meets or exceeds, that of modern mid-ocean ridge N-type basalts (MORB). AUKs are less rich in zirconium than ADKs (*12*). According to batch melting models based on the available partition coefficients [e.g., (*18*)], AUK could result from high extent of melting (~50%). The composition of AUKs from the late Archean are difficult to explain by a single melting event, as they present conflicting nonchondritic Al_2O_3/TiO_2 and CaO/Al_2O_3 ratios implying the presence of residual garnet and quasi-chondritic Gd/Yb ratio implying no residual garnet (*23*). Alternatively, a deep mantle source undergoing high extent of melting could produce a melt with high MgO content, however depleted in Al_2O_3, before the slow uplift of such melt would induce progressive enrichment in Al_2O_3 and depletion in MgO [e.g., (*2*, *12*)]. All arguments suggest AUK mantle sources considerably shallower than for ADKs. This difference, together with a lower MgO content (<30 wt%), indicates lower formation *T* for AUKs than ADKs.

3) AEKs have similar $CaO/A1_2O_3$ ratios and REE patterns to AUKs (*12*). However, they present high Al_2O_3/TiO_2 ratios ranging from the chondritic value of ~20 to as high as 50. AEKs are richer in Al_2O_3 than other komatiites and contain less MgO (>20 wt%). Accordingly, they formed by mantle melting at relatively low *P* (3 to 4 GPa), under conditions where garnet is absent from the residue. If the source were to be a mantle fertile peridotite, then the average Φ should be 30 to 40% (*26*). In terms of chemistry, AEK makes a transition from komatiites to picrites, as both compositions are similar.

Possible origin of the primitive lavas

The correlation between komatiite compositions, timing of the eruptions, and the depth of the primary sources indicates that over time, there is less magma originating from the deeper mantle regions (*19*, *23*, *27*). This evolution could be explained by the secular mantle cooling; however, this hypothesis remains partially speculative. The debate is still vivid about the magmatic processes capable of generating LIPs with large volume of mafic to ultramafic magmas in short pulses (typically less than a million years). In addition, komatiitic ultramafic lavas require large extent of melting at high *T* (*28*, *29*). The greenstone belts, for example, may represent a small fragment only of a much larger LIP (*11*). LIPs and komatiites could be associated with the rise of hot mantle plumes from the deep mantle (*30*), potentially induced by the formation of a subducted-slab graveyard (*31*). This plume could generate a positive anomaly in *T* and/or volatile element (H_2O, CO_2) concentration and favor major mantle melting. Other models propose shallower mechanisms such as mantle warming beneath supercontinents (*32*), plate-related processes (*29*), or lithospheric delamination (*33*).

The isotopic signature of LIPs and komatiites inform on the nature of their source. Similar to modern hotspots [e.g., Galapagos, Iceland, Hawaii, and Samoa (*34*)], the LIP signature overlaps with many mantle components such as depleted MORB mantle (DMM), ocean island basalts (OIB), Focal zone (Fozo), etc. (*35*). FOZO is interpreted as being located in the lower mantle (*36*). Together with high $^3He/^4He$ anomalies measured in some LIPs, it provides evidence for a source originating from deep mantle regions containing primordial ^3He (*28*). In contrast, the DMM component represents the upper mantle depleted by ~3 Ga of MORB extraction. In addition, reservoirs enriched mantle 1 (EM1), enriched mantle 2 (EM2), and hight-μ (HIMU) are likely located in the sublithospheric mantle. The overlaps found in LIPs suggest the involvement of deep sublithospheric or asthenospheric mantle components, as well as crustal or lithospheric contamination. Concerning komatiites, isotopic studies of Hf, Sr, and Nd show the overlap with the OIB component [e.g., (*37*)]. Together with high levels of He isotopes (*38*), it indicates the presence in the komatiite source of material from the deep mantle. With the high *T* required to form komatiitic magmas, this information strongly supports that komatiites formed by melting of mantle plumes coming from the very deep mantle.

Up to now, the variation of magma chemistry with *P*, *T*, and Φ is only well constrained experimentally for the first 100- to 200-km mantle depths (*23*, *39*–*44*). Higher *P* have also been investigated, however, for compositions different from those expected for the sources of LIPs and komatiites [e.g., $CaO-MgO-Al_2O_3-SiO_2$ system (*21*)] and limited ranges of Φ [e.g., around 1% (*19*)]. Previous experiments proposed global tendencies for the change of melt composition with *P* and *T*; however, the ranges of *P*-*T*-Φ covered by experimental studies remain insufficient to accurately model mantle melting at depths greater than 200 km.

RESULTS

Melting diagram of pyrolite

Solidus temperatures

To bring new constraints on the origin of LIPs and komatiites, we undertook an experimental determination of the melting diagram and of the melt composition for the first 700-km depth (i.e., ~26 GPa) for a pyrolitic mantle composition (table S1). Our experimental strategy was to synthesize samples at controlled Φ values using in situ techniques: electrical conductivity and x-ray diffraction (figs. S2 to S5 and table S2). Pyrolite solidus is found similar, within ~100 K, to the chondritic-type mantle measured with similar methods (*45*). This is substantially lower than previous reports on peridotite solidus (fig. S6) (*19*, *23*, *27*, *42*, *46*). As developed in (*45*), reasons for this discrepancy with previous works cannot be a difference in composition alone. It could result from several factors: (i) Use of simplified sample compositions, for example, CMAS (*21*). It is well accepted that additional elements induce lower solidus *T* for a typical mantle mineralogy. (ii) Use of coarse grain powders, instead of a glass sample in our study. Slow atomic diffusion may impede the formation of a solidus melt composition at grain interfaces. (iii) Lack of in situ

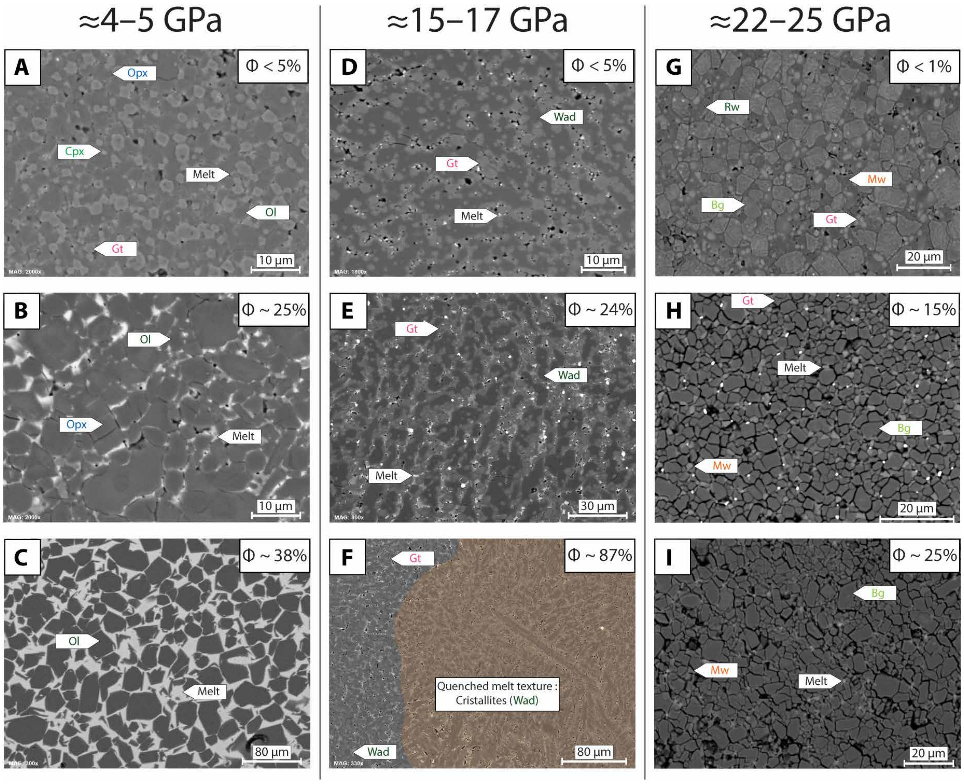

Fig. 2. Progressive increase of the extent of melting associated with disappearance of residual minerals. Left frames show experiments realised at 4 to 5 GPa, central frames 15 to 17 GPa, and right frames 22 to 25 GPa. (**A** and **B**) *MA105*, (**C**) *T2*, (**D**) *MA119*, (**E** and **F**) *MA116*, (**G**) *MA149*, (**H**) *MA143*, and (**I**) *MA144*. At *P* around 4 to 5 GPa, several mineral phases [clinopyroxene (Cpx) and garnet (Gt)] disappear at small extent of melting. With increasing *T*, orthopyroxene (Opx) is enriched in compatible elements (i.e., MgO) and presents grain size exceeding that of olivine. At higher *T*, melting of Opx is associated with a major growth of olivine grain, which is the liquidus phase. At *P* around 15 to 17 GPa, wadsleyite (Wad) and garnet continue to coexist up to very high melting extent. Garnet appears to be the liquidus phase of pyrolite at *P* > 15 GPa. For *P* > 22 GPa, ringwoodite (Rw) and garnet disappear at a relatively low concentration (<25%). After that, bridgmanite (Bg) starts to melt and ferropericlase (Mw) becomes the liquidus phase.

melting criterion and characterization method insufficiently sensitive to detect thin melt films in the recovered samples. Small pockets of melt can be destroyed during the polishing steps. In addition, melt films can be difficult to identify using the scanning electron microscope (SEM) (*47*). (iv) Last, important thermal gradient within the sample charge can lead to *T* and Φ errors.

Apart from (*45*) that is in good agreement with our melting curves, none of the studies cited above used in situ techniques to detect the onset of melting (such as electrical conductivity and x-rays), and none probes the evolution of Φ at higher *T* (such as a falling sphere). In previous works, melting was generally detected on the basis of "trials and errors" and the solidus and liquidus *T* were sometimes identified using the *T* gradient in a single sample. However, major thermal gradients induce melt migration; the presence of chemical gradients within the capsule disables the determination of the melting behavior of the starting material. For example, a solid residue identified in an unmelted zone of the sample can result from the compaction of refractory minerals, which melting *T* can be far above the solidus and liquidus of the bulk composition.

Extent of melting

To probe the melting properties at higher Φ, we developed an original falling sphere technique to detect in situ the occurrence of the rheological transition upon heating (fig. S5). When Φ becomes 30 to 40%, a Re sphere falls at an irregular speed in the melt located between the solid grains. It indicates the change of rheological behavior from solid type to liquid type (*48*). The samples were quenched at the rheological transition or at a slightly higher *T* on the basis of thermocouple reading. The extent of melting was determined for each sample by numerical analyses (Fig. 2 and fig. S7). To achieve a maximum precision, we correlated backscattering electron images and chemical maps obtained by SEM; melt regions present a maximum concentration of incompatible elements. A rapid increase of Φ up to 30 to 40% melt within the first 100 K above the solidus was observed (Figs. 3 and 4). Then, Φ increases less steeply at higher *T*. At high extent of melting, the grain size of the residual solid phases becomes 10 to 30 μm or more, with well-developed polygonal textures, especially for olivine, orthopyroxene, and bridgmanite.

Liquidus temperatures

Liquidus *T* can primarily be constrained on the basis of the extrapolation to 100% of the relationship between Φ and *T* (Fig. 3). Additional constraints come from *T* measured for (i) very fast and linear trajectory of the falling sphere indicating the absence of solid grains [such as in (*49*)] and (ii) complete disappearance of x-ray diffraction peaks from the sample. (iii) We also monitored the reappearance of crystallites upon cooling and (iv) microstructure of a number of "trial and error" syntheses at variable *T*, indicating whether the sample has been fully molten or not. All evidences converge on a pyrolitic-mantle liquidus 275 ± 50 K higher than the solidus at all upper mantle depths. Our experiments are compatible with previous works showing that for the pyrolitic/peridotitic composition, majorite replaces olivine at the liquidus between 13 and 16 GPa, and ferropericlase replaces majorite at ~22 GPa (table S3) (*19*, *23*, *46*).

Comparison between experimental melts and natural lavas

Chemical compositions of the melts were determined using the electron microprobe (Supplementary Materials, Figs. 5 and 6, fig. S8, and table S4). From the correlation between Al_2O_3 content and CaO/Al_2O_3 ratio in experimental melts (*19*, *23*), three major trends arise: (i) High extent of melting yields low CaO/Al_2O_3 ratio and low Al_2O_3 content. The pyrolitic melt (i.e., Φ =100%) presents CaO/Al_2O_3 ~ 0.45 and Al_2O_3 ~ 4.5 wt%. (ii) Low P favors high Al_2O_3 content and (iii) high P favors high CaO/Al_2O_3 ratio. In this figure, we superimpose a compilation of the composition of numerous basalts, picrites, and komatiites of different ages and locations. The domains where the different LIPs and komatiites overlap with experimental melts provide strong constraints on their mantle origin (see the Supplementary Information for a discussion of the role of alteration on the CaO/Al_2O_3 ratio in LIPs and komatiites).

The comparison suggests a minimum depth of 550 to 600 km (20 to 23 GPa) to produce the old ADK (Fig. 6). Their compositions

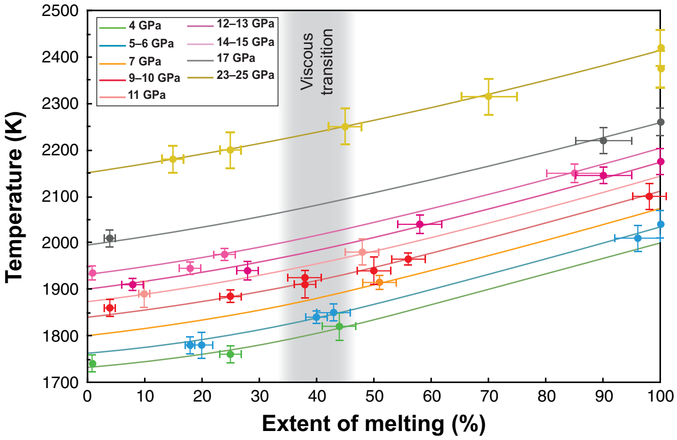

Fig. 3. Temperature dependence of extent of melting. The volumetric extent of melting (Φ) is determined at various *P* and *T* on the basis of the joint analyses of electron microphotographs and chemical maps of the recovered samples. High melting extents are also constrained from mass balance calculations. Extrapolation to Φ = 100% of the quasi-linear relation found at high Φ yields a good estimate of the liquidus *T* as a function of *P* (distinguished by colors).

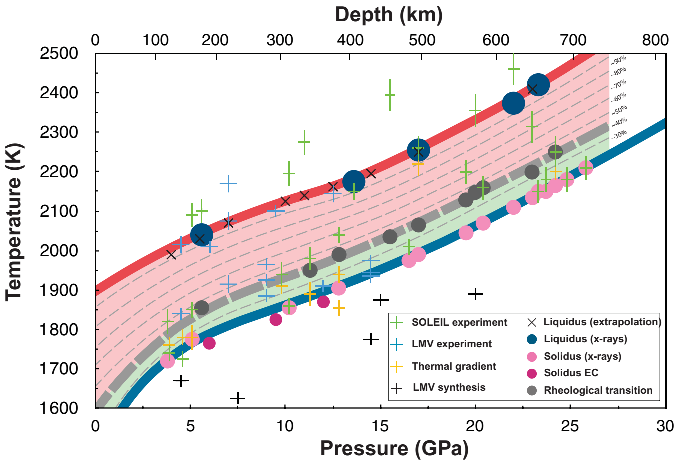

Fig. 4. Melting diagram of the pyrolitic mantle. The solidus is determined up to 25 GPa using in situ electrical conductivity (red circles) and x-ray diffraction (pink circle). The rheological transition at 30 to 40% of melt (gray dashed line) and the liquidus are determined using various methods, including a new falling sphere technique (Supplementary Materials). Both solidus and liquidus present a change of slope at ~15 GPa, when the high-*P* polymorphs of olivine become stable.

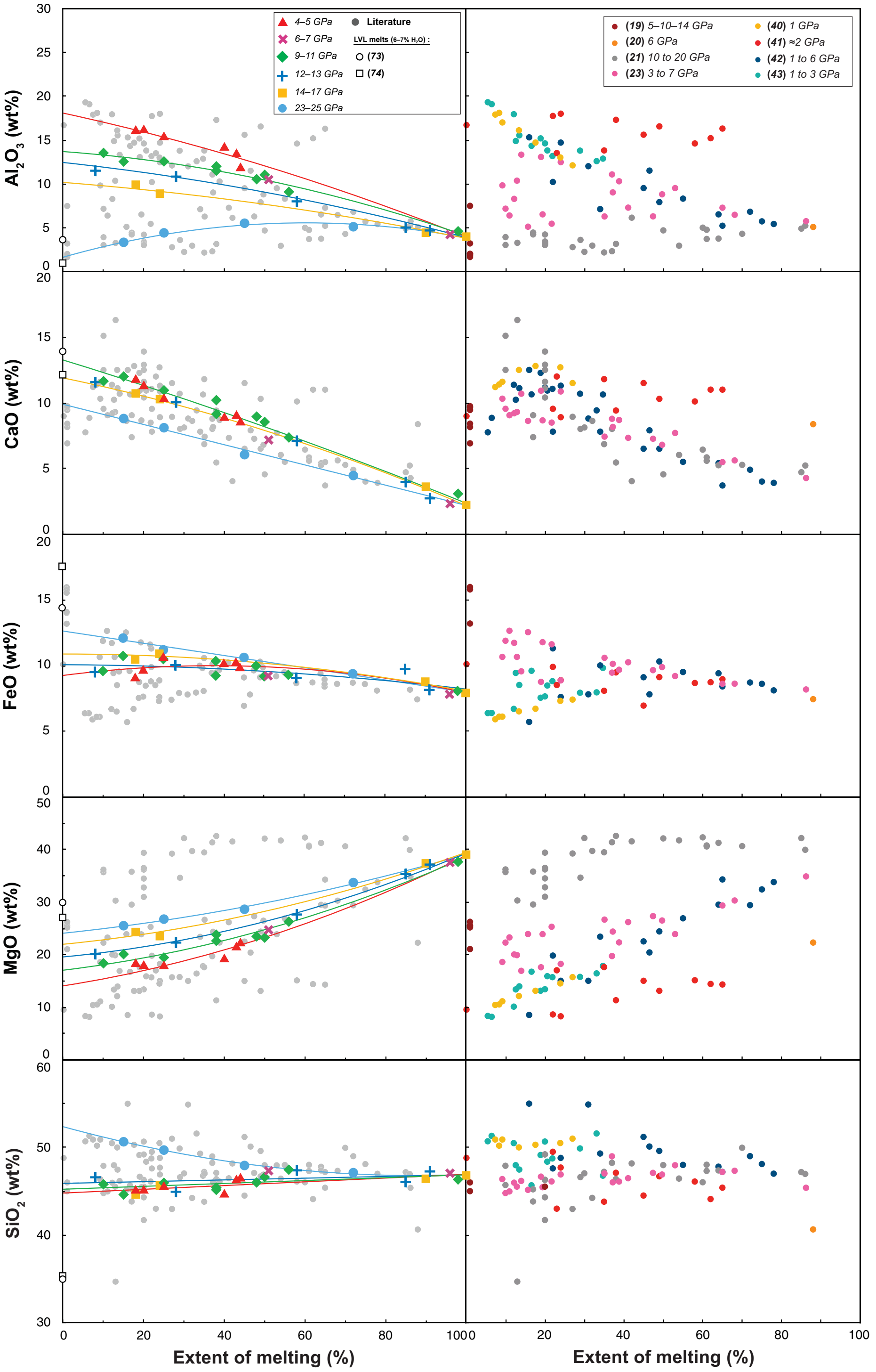

Fig. 5. Variation diagrams showing oxide abundances of melt versus extent of melting (wt%). (**Left**) Chemistry of our melts at various pressures and degrees of mantle melting. Averages of several electron microprobe analyses in the melt regions of our samples are plotted as colored symbols, for *P* between 4 and 25 GPa. One SD is <5% for each melt composition. (**Right**) Chemistry of melt's literature at various pressures and degrees of mantle melting. Each color represents a different study for the pyrolitic/peridotitic upper mantle: (*19*, *21*, *23*, *39*–*44*).

overlap with melts at Φ values ranging between 10 and 25% and 20 and 50% for highest and lowest *P* (thus with decreasing CaO/Al_2O_3 ratio), respectively. The presence of residual Al-bearing garnet at moderate *P* can induce low Al content in the melt. However, the CaO/Al_2O_3 ratio cannot be very high in this case because garnet also incorporates CaO easily. At lower mantle pressures, bridgmanite and davemaoite (Dvm; $CaSiO_3$-perovskite) are rich in Al and Ca, respectively. Melting of Dvm above solidus yields primary melts enriched

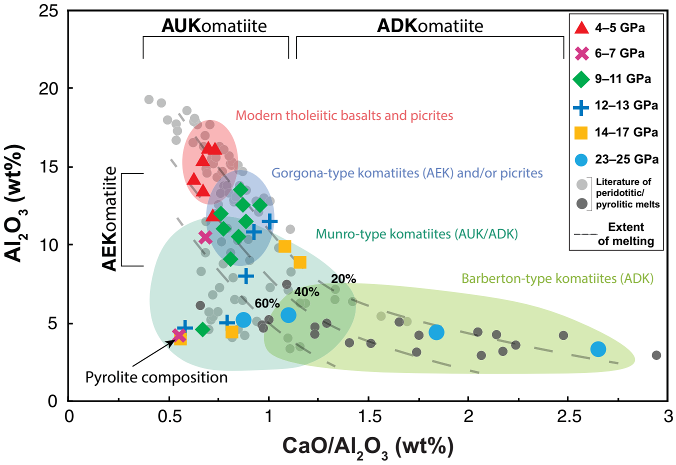

Fig. 6. Correlation between Al_2O_3 contents and CaO/Al_2O_3 ratio of experimental melts and natural lavas. Melt compositions are regrouped by experimental *P* ranges (colored symbols). We also report melt composition from previous experimental reports: Light or dark gray circles indicate studies reproducing the CaO/Al_2O_3 ratio from melting of peridotite/pyrolite under mantle relevant (*23*, *27*, *39*–*43*, *46*, *79*) or more specific (*19*–*21*) experimental conditions, respectively. Colored areas correspond to natural lavas of Barberton-type (ADK, light green), Munro-type (AUK, dark green), Gorgona-type (AEK), and ancient (blue) and recent (red) picrites and basalts [see (*54*)]. On the basis of the degree of partial melting (Φ) measured in our samples (Fig. 3), we draw contour lines corresponding to Φ ~ 20, 40, and 60% (dashed gray lines). Comparing the composition of LIPs/komatiites of different ages (fig. S1) and experimental melts at varying *P* and Φ indicates the mantle source for each type of lava.

in CaO and poor in Al_2O_3. In these mantle conditions, melts with high MgO and SiO_2 contents and high CaO/Al_2O_3 ratios can be produced at relatively low extent of melting. These results are in relatively good agreement with previous works (*22*–*25*), including (*50*) that suggests that komatiite genesis involves a high extent of melting (>30%) at low *P* < 5 to 6 GPa, after adiabatic decompression of mantle diapirs that begin to melt in the transition zone (*P* > 15 GPa) or at even higher depth (*P* > 20 GPa). In all cases, T_p at the time of ADK formation should be appreciably higher than that prevailing today (*1*).

The intermediate position of AUK suggests mantle sources of 300- to 550-km depth (i.e., 10 to 20 GPa), as proposed previously [e.g., (*19*, *23*, *27*)]. To produce Al-undepleted melts, the presence of a residual garnet is not mandatory. There is a smooth transition between the ADK and AUK between 20 and 25 GPa, which explains the coexistence of AUK and ADK in some Munro-type outcrops. Because of similar sources, the two melts present similar major element contents, but the *P* difference can still induce substantial differences in minor and trace elements. Formation of the AUK occurred primarily during the Late Archean and could therefore correspond to lower *T* than the Barberton komatiites (*11*, *12*). On the basis of our experiments at AUK, lavas are compatible with Φ from 15% to more than 60%, which makes AUK compositions quite close to bulk pyrolite. AUK can be produced in a wide range of *P* from ~5 to 10 GPa to ~25 to 30 GPa, when Φ is very high (>50%).

AEK, picrites, and basalts align along near-vertical trends at CaO/Al_2O_3 ratio between 0.5 and 1 and with Al_2O_3 contents varying from ~8 to ~17 wt%. AEK can be produced by melting at 200- to 400-km depth [i.e., 7 to 13 GPa, in agreement with (*2*, *19*, *23*)] and picrites and basalts at 100 to 200 km (i.e., 4 to 5 GPa). Our results suggest moderate extent of melting (Φ < 50%) for recent Gorgona-type komatiites and picrites; melts enriched in Al_2O_3 suggest mantle melting without garnet in the solid residue. Last, picritic and basaltic lavas, which represent LIPS and recent hotspots such as Hawaii or Reunion Island, correspond to melting extents lower than 30% (*2*, *17*).

The melt contents in other major elements confirm the trends presented above. We draw correlation diagrams between them, which show the effect of *P* on the melt composition (Fig. 5). The bulk sample composition, pyrolite, is a singular point in these diagrams because the melt composition evolves toward it with increasing Φ, irrespective of the experimental *P*. On these diagrams, we superimpose the compositions previously reported for basalts, picrites, and komatiites (fig. S8): (i) CaO versus SiO_2 diagram. The high SiO_2 content obtained at the highest experimental *P* and moderate Φ explains well the composition of ADKs. (ii) Al_2O_3 versus CaO and Al_2O_3 versus MgO diagrams. At relatively low Φ (i.e., at high CaO or low MgO content), the sequence of natural lavas (ADK, AUK, AEK, and picrites/basalts) is well compatible with the *P*-induced decrease of Al_2O_3 content in melts (Fig. 5). (iii) CaO versus FeO diagram. The increasing FeO content with increasing *P* at relatively low Φ is also well compatible with the sequence of natural lavas.

DISCUSSION

Mantle conditions for the origin of LIPs and komatiites

We now combine the evolution of Φ between the solidus and liquidus of pyrolite at various mantle depths (from Fig. 3) with the chemical overlap between experimental melts and natural lavas (from Fig. 6). The result (Fig. 7) highlights the likely source region for primary magmas at the origin of LIPs and komatiites. In addition, we plot, the current mantle geotherm (*51*) and its range of uncertainties (gray area), as well as mantle geotherms with T_p 100, 200, and 300 K higher than today (gray lines) (*1*). We acknowledge that these *T* profiles do not formally correspond to mantle *T* profiles; as they go through regions between the solidus and liquidus, the effect of latent heat of mantle fusion should be included. Still, the mantle depth at which an adiabatic profile crosses the solidus informs truthfully on the onset of mantle melting along a decompression path. It appears clear that T_p > 200 to 300 K higher than today induces melting in the *P* domain corresponding to ADK. Secular mantle cooling can explain the progressive disappearance of ADK, with preservation of AUK lavas when T_p was >150 to 200 K above that prevailing today (Fig. 1). Last, a mantle plume >50 to 150 K hotter than the average mantle would yield the production of picrites and deep basalts, which are currently found at oceanic islands (e.g., La Reunion) and mid-oceanic ridges, as well as AEK. These hot mantle plumes could still be uprising today (*52*), producing supervolcanoes like Toba (Indonesia) or Yellowstone (the United States).

Previous works were based on the modeling of mantle cooling using the Urey ratio (*53*) or thermodynamical modeling using the PRIMELT method (*1*, *3*). Other less extreme scenarios exist on the basis of similar calculation from the Urey ratio or petrological modeling technique to derive primary magma compositions using large datasets of non-arc basaltic lavas (*9*, *54*, *55*). Our estimates of Archean temperatures are in better agreement with the most recent studies. These discrepancies can be explained by several critical points in the thermodynamical calculations. Different petrological models give different parameterizations for the MgO content in the melt

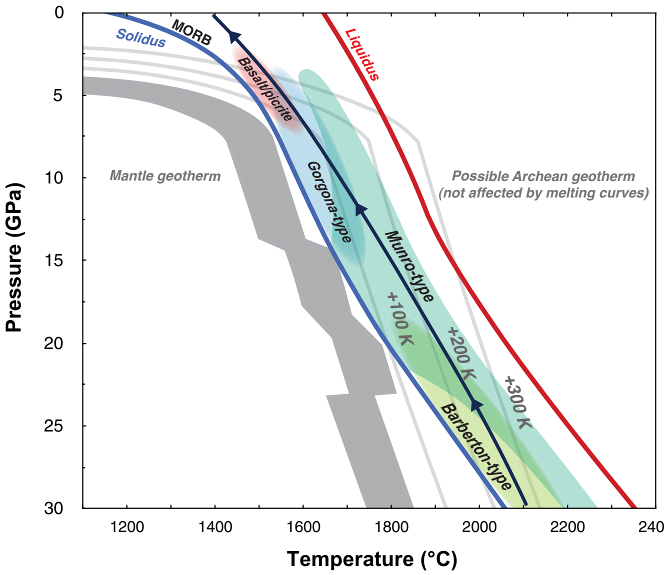

Fig. 7. Mantle *P*-*T* regions are sources of the different LIPs and komatiites. Solidus (blue line) and liquidus (red line) of pyrolite are reported together with the current mantle geotherm (gray zone), and *T* profiles that are 100, 200, and 300 K higher than the geotherm (light gray lines; these *T* profiles are not corrected for the effect of latent heat of fusion between the solidus and liquidus). Φ values between solidus and liquidus are constrained from our experiments (Fig. 3). The likely source region of the different types of lavas is determined on the basis of their composition (Figs. 5 and 6). The low-*P* basalts and picrites plotted in the figure correspond to flood basalts and OIBs found in the Phanerozoic. MgO-rich picrites (i.e., corresponding to higher *P* and melting extents) found on the islands of Gorgona and Curaçao present a chemistry close to komatiites and are therefore classified in the Gorgona-type group. The thicker blue line serves as a guide to the eyes for the ascent of a hot mantle plume that could be the origin of the oldest komatiites (see Fig. 8).

produced by decompression melting, as a function of *P* and *T* [e.g., (*56*)]. The thermodynamical models rely heavily on the available experimental data, and before our work, these data were limited to *P* below 7 to 8 GPa concerning the formation of high MgO magmas (*2*, *23*). We show that Archean komatiites can be produced at higher *P* than previously thought. A major reason of this discrepancy is our lower solidus profile; it yields differences of 100 to 200 K lower than previous works for the T_p value of the primitive mantle. In addition, we provide an accurate determination of the rate of melting as a function of *P* and *T* for the anhydrous mantle. This yields a more accurate dataset on the melt chemistry over a wide range of mantle *P*-*T*. Still, we observe relatively good agreement with the literature, indicating that the key point is the accuracy of the *T* measurement within the sample, and the relationship between melting rate and *T* between solidus and liquidus.

Which mantle thermal state produces primitive ultramafic magmas?

The production of a large volume of mafic to ultramafic magma is generally explained by the rising of a hot mantle plume (*29*, *30*). However, if the mantle *T* profile follows an adiabatic gradient [corresponding to T_p of 1600 K or higher (*57*)], then substantial thermal anomalies can only be generated if the ascending material comes from the hot thermal boundary layer in contact with the core. Such mechanism can explain the present-day OIB (*28*, *58*); the hot material can eventually form a dome and rise toward the surface. Still, the thickness of the hot-layer atop the core-mantle boundary (CMB) could only be several hundred kilometers, yielding mantle plume with a reduced volume. These smaller plumes are unlikely to generate great LIPs.

T_p higher in the past than that prevailing today would yield ubiquitous and persistent mantle melting in a wide range of mantle depths (Fig. 7). This thermal state is not consistent with the sporadic character of the LIPs. In addition, if the extent of melting should become larger than ~40%, as required to explain the composition of some komatiites, then this would indicate a layer of very low viscosity within the upper mantle for a very long time, which is a new concept with implications to be investigated. Last, warmer adiabatic *T* profiles with a mushy upper mantle are not found in line with the cooling history of Earth, when the starting point is the MO solidification after the Moon-forming impact [see e.g., (*59*)]. Alternatively, major thermal anomalies within the deep mantle could more simply explain the properties of LIPs and komatiites.

The simplest mechanism to produce large mantle plumes with positive *T* anomalies is a superadiabatic *T* profile in the deep solid mantle (Fig. 8). This favors mantle instabilities and overturns; large volumes of deep mantle can rise to the surface and become hotter than the surrounding mantle because they cool less during the adiabatic decompression than the superadiabatic gradient prevailing in the mantle. We recently demonstrated that super adiabatic gradients should prevail in the deep mantle for 1 Ga or more after the major Moon-forming impact (*59*). This thermal state is a necessary step between (i) the solidification of the global magma ocean, which yields a *T* profile close to the mantle solidus and (ii) the adiabatic profile of the present-day mantle with T_p of 1600 to 1650 K (if an adiabatic *T* gradient is really achieved today). Along this cooling stage, *T* should decrease by 500 to 1000 K in the lowermost mantle. It implies the extraction of a huge amount of heat, especially because of other sources of energy available, such as radioactive disintegration.

Superadiabatic mantle gradients could be at the origin of LIPs

Following previous work (*59*), we recalculate the evolution of the mantle *T* profile over time after the crystallization of a pyrolitic magma ocean. A most appreciable difference in the parameters is the solidus of pyrolite, which presents a progressive increase with increasing depths in the upper mantle (fig. S6). Because of this curvature, the last mantle region to solidify upon cooling is at mid-upper mantle depths (fig. S9), instead of just below the surface for the chondritic-type mantle composition used in the previous work. It results that the cooling rate of the pyrolitic mantle is significantly slower, with a *T* profile remaining largely superadiabatic in the deep mantle for 2 to 3 Ga or more (Fig. 8 and fig. S9). Together with the fact that melting happens solely in the first 1000 km of the mantle (fig. S12), such long time scale provides a primary justification for using the properties of the pyrolite mantle for our discussions; while the bulk primitive mantle could very well be of chondritic-type composition after the core segregation, the mean mantle involved in the convection processes 2 to 3 Ga later in the shallow mantle is believed to be similar to pyrolite composition.

We also calculate the *P*-*T* path that uprising material would follow along adiabatic decompression paths, taking into account the latent heat of fusion [e.g., (*50*)] when the plume enters the *P*-*T* domain between the solidus and the liquidus. The adiabatic uprising

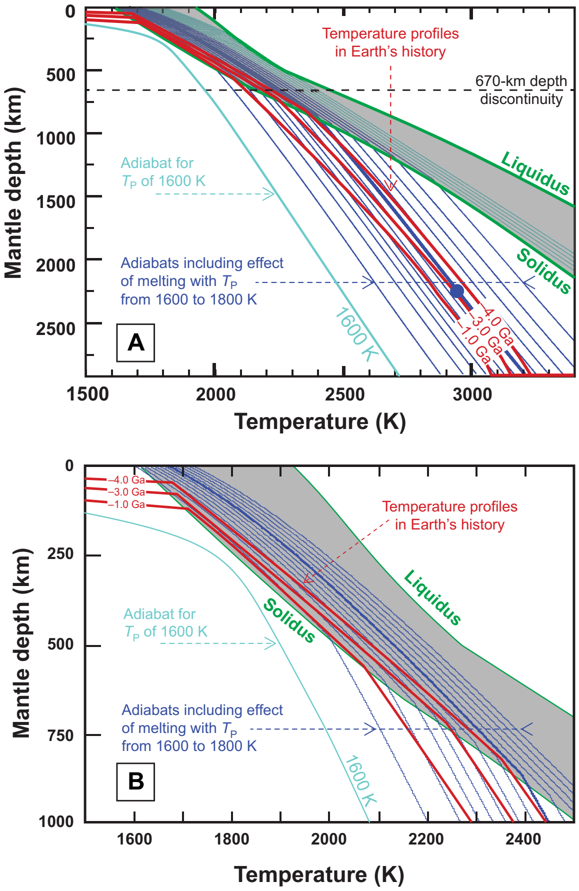

Fig. 8. Thermal state in the ancient mantle. Panel (**A**) reports the solidus and liquidus of the pyrolitic mantle (green lines), the present-day reference adiabatic T gradient for Tp = 1600 K (light blue), ancient adiabatic T gradients going through a mushy zone in the upper mantle (blue lines), and ancient T profiles with ages from 4.0 to 1.0 Ga before present (red lines). Panel (**B**) is a zoom of the figure A between 0 and 1000 km and 1500 to 2500 K. The T profiles result from modeling the cooling of a pyrolitic mantle composition from a global magma ocean, following previous work (*59*). The thicker blue line is a guide for eyes for the ascent of a hot mantle plume. With an initial temperature typical of an ancient T profile, for example, 2850 K at 2300-km depth in a ~3-Ga-old mantle [blue dot in (A)], a rapid decompression path along its corresponding adiabatic T gradient (bold blue line) yields a mantle plume with a major T excess in the shallow mantle, compared to the average T profile. This plume would cross the solidus at ~800-km depth and melt partially at levels of 25 to 30%, ~50%, and 30 to 40%, at mantle depths of 660 km, 300 to 500 km, and 100 to 200 km, respectively. This information is given by the position of the thick blue line between the solidus and liquidus in (B), following the expected extent of melting as a function of P and T (Fig. 3). These conditions are compatible with the formation of Barberton-type komatiites (Fig. 7). Our model of liquid komatiite petrogenesis by adiabatic decompression is similar to that of picrite or MORB petrogenesis, except that it involves a superadiabatic T gradient to generate hot mantle plume coming from great mantle depths.

of a mantle blob from 2300-km depth and 2850 K (which corresponds to mantle conditions about 3 Ga ago; blue dot in Fig. 8) would cross the solidus at ~800-km depth and melt partially at levels of 25 to 30%, ~50%, and 30 to 40% at depths of 660 km, 300 to 500 km, and 100 to 200 km, respectively (fig. S8). These melting conditions are very compatible with those needed to produce ADK, AUK, and early AEK-picrite lavas, respectively (Fig. 6). Therefore, the prevalence of superadiabatic gradients in Archean and early Proterozoic mantle offers new explanations for the sources of LIPs and komatiites. Within the first ~1000-km depth, the magnitude of the *T* excess of the mantle plume, compared to the average mantle, depends on the level of mantle superadiabaticity of the *T* profile in the deep mantle and the depth from which the mantle plume originates. With secular cooling, the level of superadiabaticity decreases, inducing smaller *T* anomalies in the shallow mantle.

Another major aspect that still needs to be addressed is the volume of uprising material, which needs to be several million cubic kilometers to produce major LIPs. While the presence of superadiabatic mantle gradients could provide an explanation for the presence of hot plumes in the upper mantle, the dynamics of such hot mantle could be different from today. A steep *T* profile in the past implies high Rayleigh number value and turbulent mantle convection. Unsteady convection cells could have developed with characteristic length scales much smaller than the mantle thickness (*60*). At early time, uprising of hot material from the deep Earth may have occurred sporadically along heat pipes (*61*). Mantle cooling over the Hadean and the Archean should have progressively increased the length scale of mantle convection, due to the decrease of the Rayleigh number, before global mantle convection is progressively established (*62*). Under these circumstances, the production of LIPs and komatiites and slab subduction would be precursors of the establishment of global mantle convection prevailing in modern Earth.

MATERIALS AND METHODS

Sample preparation

As starting material, we used a typical composition of pyrolitic mantle. This model is constructed by adding some MORB to mantle peridotite. It is dedicated to represent a primitive undepleted upper mantle (*63*). Our pyrolitic composition (table S1) is not far from KLB-1 (*27*) and fertile oceanic peridotites (*64*). A mixture of synthetic powders was homogenized in an agate mortar, before glass spheres of diameter ~2.5 mm were produced using an aerodynamic levitation system (*65*). The use of a regulated flow of pure Ar yields a convenient $Fe^{3+}/(Fe^{2+}+Fe^{3+})$ ratio of 7 to 8% for such type of sample composition (*66*).

We determine the water content in the pyrolitic glass using infrared spectroscopy, based on the Beer-Lambert law and absorption coefficients given for basaltic (*67*) and basanitic (*68*) glasses. These coefficients are valid when using the height of a water band located at, e.g., 3450 cm^{-1}. With water contents ranging between 18 and 22 parts per million, we consider the glass starting material nominally dry.

Glass spheres are reshaped by polishing in the form of a cylinder to be directly inserted in the high-*P* assembly of the multi-anvil press (MAP). The cylinder of glass offers several advantages including a rigid shape during compression and a very small surface/volume ratio for moisture absorption, compared to powders. We keep the sample length less than 1 mm to reduce *T* gradients during high *P* and *T* experiments.

Electrical conductivity measurements

Electrical conductivity measurements are performed up to 20 GPa at the Laboratoire Magmas et Volcans using the same experimental procedure as in our previous work (*45*). We use tungsten carbide cubes with edge truncation of 11, 6, or 4 mm, octahedron *P* medium made of Cr_2O_3-doped MgO with edge length of 18, 14, or 10 mm, respectively, and cylindrical furnace made of a Re foil of 25-μm thickness. The heater is surrounded by a zirconia sleeve, which serves as thermal insulator. The sample is inserted in an MgO capsule; MgO is softer than alumina parts, which minimizes the deformation of the molten sample. Before preparation of the assembly, all ceramic parts are fired at 1000°C for 1 hour and stored in a vacuum furnace at 150°C together with the glass sample. The sample length is determined before and after the experiment using a high-precision digital gauge and the SEM. We apply a correction based on elastic parameters to account for the change of sample length due to compression and thermal expansion. *P* is determined on the basis of a press-load versus sample-*P* calibration using the well-known phase transition in mantle minerals. The uncertainty evolves from 0.5 to 1 GPa with increasing *P* (*69*).

Rhenium disks electrodes with diameter of 1 mm are positioned at the top and bottom of the sample. They maintain the electrical connection between the sample and the electrodes and favor the spreading of the current at the sample surface. On one sample side, we insert the two wires of a C-type thermocouple ($W_{0.95}Re_{0.05}$-$W_{0.74}Re_{0.26}$) through the MgO cylinder and in contact with the Re disk. A third $W_{0.95}Re_{0.05}$ wire is positioned at the other sample side. On the basis of this configuration, the sample *T* can be measured on one sample side and impedance spectra are collected between the two $W_{0.95}Re_{0.05}$ wires. Because of the proximity with the Re furnace, we estimate our sample fO_2 close to the Re-ReO_x buffer.

Absence of a metallic capsule around the silicate sample can induce the escape of some melt from the sample core, especially when achieving high extent of melting. This melt could react with the MgO sleeve. Fortunately, this effect is reduced when a stronger cohesion of the cell assembly is achieved at high *P* (*70*). In addition, we perform fast heating after the solidus *T* is detected (see below). Using the trial-and-error method, we optimized the experimental duration to obtain a good textural and chemical equilibrium together with minimum melt migration.

Electrical impedance of samples was recorded using the ModuLab MTS Impedance/Gain-Phase Analyzer in a range of frequencies between 1 MHz and 1 Hz [see details in (*45*)]. After compression to the target *P*, we performed different cycles of heating and cooling to remove adsorbed moisture from the assembly components, until a reproducible sample conductivity is achieved. Then, *T* is raised up to ~1300 K, which is above the glass transition of our pyrolite glass. The sample resistivity increases again as a sign of final dehydration and crystallization. The grain size is up to 2 to 10 μm, based on the microstructure of quenched samples. After this step, the sample is cooled to 600 to 800 K before the final heating up to the melting *T*. Our major criterion for the detection of solidus is the change of slope in the *T* dependence of sample conductivity (fig. S4).

X-ray measurements

We performed x-ray diffraction and contrast imaging in situ in the MAP operating at the PSICHE beamline of the SOLEIL synchrotron using the same experimental procedure as in our previous work [see details in (*45*)]. *P* up to 27 GPa is generated using WC cubes with 3- or 4-mm truncation edges mounted with 7- or 10-mm-length Cr-doped MgO octahedra. High *T* is provided by a Re tubular furnace surrounded by a ZrO_2 sleeve for thermal insulation. Re electrodes with a donut shape are used to connect each furnace extremity to one cube truncation. Heating is obtained by applying an alternating current at 100 Hz.

T is monitored by a C-type thermocouple (W/Re) in contact with the furnace at the center of the assembly. All pieces are positioned horizontally in parallel with the x-ray beam.

The beamline configuration is similar to that for a previous study dedicated to measuring the silicate melt viscosity (*49*). At the sample position, we use either (i) a relatively large beam of about 2 mm by 2 mm to record the sample image as a function of time using a fast charge-coupled device camera (>100 frames per second) located behind the MAP or (ii) a beam collimated to 50 μm by 200 μm to characterize the sample mineralogy and monitor *P*. X-ray diffraction patterns are recorded in energy-dispersive mode using a Ge solid-state detector coupled to the Caesar-type diffractometer. A 2θ diffraction angle of 8.0° ($\pm 10^{-3}$) is convenient to register the major diffraction lines of our silicate samples. On the basis of uncertainties of the determination of the MgO cell parameter and on the MgO equation of state itself, the uncertainty in the *P* determination is ~0.3 GPa (*71*).

The new falling sphere technique

We investigate the rheological transition occurring in the sample at an extent of melting (Φ) of 30 to 40% using x-ray imaging and an original "falling sphere" method (fig. S5). For this, using laser ablation, we drill a small hole on the lateral surface of the cylindrical sample at equal distance from the two ends. One or two rhenium spheres with diameters of 50 to 80 μm are inserted in the hole. We verify that Re spheres are located on the upper side of sample when inserting the assembly in the MAP. The sample *P* is determined on the basis of the x-ray diffraction signal of the MgO disks located on each side of the sample.

Upon heating above the solidus, we first observe some instabilities in the position of the sphere likely produced by an increasing Φ in the sample. With further *T* increase, the sphere starts to fall within the sample. Its movement appear to be chaotic, indicating the sphere bouncing on the surrounding mineral grains. The sphere does not fall at a constant speed and takes several seconds to go across the sample. Its complete fall takes orders of magnitude longer than a sphere fall through a fully molten sample at similar *P* (*49*). The slow falling of the sphere evidences a rheological transition between solid-like to liquid-like behavior. This transition occurs when the amount of melt is sufficient to disrupt the rigid cohesion between grains forming the solid matrix. Still, the high fraction of solid grains prevents a rapid fall of the sphere. We have heated some of our samples to even higher *T*, and in this case, the sphere falls through the entire sample in milliseconds (~200 ms). Using this technique, we have monitored the rheological transition at eight different *P* from 5 to 24 GPa and at *T* ranging from ~1855 to ~2250 K (table S2) The extent of melting is determined a posteriori on the recovered samples.

Temperature gradients and uncertainties

Estimation of thermal gradients is crucial for an accurate determination of the pyrolite melting *T*. They can yield to heterogeneities in partially molten samples, although the sample volume is less than 1 mm^3. Our recovered samples do not present significant zoning when using the 18/11 cell assembly, neither in Φ nor in the chemical composition of the different phases. The situation is not as ideal when using the smaller 14/6, 10/4, or 7/3 assemblies. We limit artifacts possibly generated by chemical segregations by duplicating experiments several times and crosschecking the petrological and chemical analyses of different samples. For a few samples, the texture and sample mineralogy were slightly different at the two capsule ends because of non-negligible T gradients. If the overall chemical homogeneity is well preserved, then these samples can still be used to determine the melt composition, based on chemical analyses of the different sample areas.

We model the T field for our different cell assemblies for thermocouple readings between 1773 and 2273 K (fig. S10) (*72*). We obtain a T difference of less than 100 K between the sample and the thermocouple located in contact with (i) an electrode at the top of the sample for electrical conductivity experiments and (ii) the tubular furnace around the sample for x-ray experiments. The difference can only be higher if the sample is significantly off the center of the assembly (and especially for 10/4 and 7/3 assemblies), which can be checked on the recovered samples. The coldest zones are the top and bottom of the cylindrical sample, while the central plane of the sample records the highest temperatures. We applied a correction to all T measurements based on the modeled T gradients.

For conductivity measurements, the sample volume is ~0.8 mm^3 and maximum T difference of 60 or 70 to 80 K is calculated using 18/11 or 14/6 and 10/4 assemblies, respectively. For x-ray measurements, maximum T difference is 80, or 90 K, for 10/4 assembly with a sample volume of 0.4 to 0.5 mm^3, or 7/3 assembly with a sample of 0.2 to 0.3 mm^3, respectively.

Microstructure of recovered samples

Texture and mineralogy of recovered samples is characterized using the SEM. Samples are mounted in an epoxy resin and polished to mirror-like surface. Longitudinal section (along the furnace axis) is the most convenient to check the sample homogeneity and estimate the extent of melting and abundance of the different minerals. Observations are carried out using both JEOL (JSM-5910 LV at LMV) and field-emission gun ZEISS (supra 55VP at 2MAtech, Aubière, France) SEMs with accelerating voltage of 15 kV and working distance (WD) from 6 to 11.6 mm. The use of small WD enables the detection of small veins of melts typical of low Φ.

Observations confirm that the initial shape of the samples is well preserved, even at high melting extents. Images show a good textural equilibrium for all our samples, based on well-crystallized polygonal grains with diameters of several micrometers and grain boundary angles close to 120° (Fig. 2 and figs. S3 and S7). The particles size does not change significantly with P but rather with increasing T. The presence of cracks in some samples could result from tensile stresses during quench and decompression.

Several chemical maps (Si, Fe, Mg, Ca, Al, and K) have been recorded using energy-dispersive spectroscopy to image the elemental distribution between the melt and the solid residue. Mg, Al, and Si provide a rapid identification of major minerals; olivine and its high-P polymorphs, pyroxenes, and garnet. Fe, Ca, and K provide clues for the identification of the network of melt pockets.

Determination of the extent of melting

We use high-resolution electron microphotographs to determine Φ in our samples. At the solidus T, samples show nanometric traces of melts at the grain triple junctions and along grain boundaries. In this case, the size of melt pockets or films is generally too small to enable a precise measurement of the melt composition, due to chemical interferences with the adjacent minerals. At T of 20 to 50 K or more above the solidus, the interconnected melt presents a very low dihedral angle (fig. S3). To prevent artifacts in the determination of Φ, we used the MATLAB software to correlate the backscattered electron images with chemical maps of the incompatible elements, which present a maximum concentration in the melt regions. We perform several calculations with adaptable pixel sizes to check the robustness of our method; uncertainties on calculated Φ are <2 and <5% for low and high extents of melting, respectively (Fig. 2 and table S3). These Φ values are in very good agreement with other Φ values calculated on the basis of the chemical composition of all the phases coexisting in a same sample. Still, the mass balance technique provides larger uncertainties compared to image analyses. When a thermal gradient is detectable inside a sample, the extent of melting is studied in the different regions and the T in each zone is estimated from modeled T gradients (fig. S10).

Chemical analyses

Chemical compositions of melts are determined by electron probe microanalyses. We used alternatively Cameca SX100 and SXFiveTactis electron probes with a same accelerating voltage of 15 kV and a beam current of 20 nA. Quantitative analyses are obtained for eight elements (Si, K, Fe, Na, Ti, Al, Ca, and Mg) with counting times of 20 s on peak maxima and 2 × 10 s on the background. As standards, we use natural minerals and synthetic oxides (Si and Ca, wollastonite; Mg, forsterite; Al, Al_2O_3; Fe, fayalite; Na, albite; K, orthoclase; Ti and Mn, $MnTiO_3$; Cr, Cr_2O_3; and Ni, NiO) and pure metal (Fe, Mn, Mg, Ni, and Cr) for metal alloys. Mineral phases and vein of melts are analyzed with a focused beam (2 to 5 μm), while large melt pools (with texture of quench) are analyzed with a beam defocused to diameter of ~10 μm. In this case, standards are also analyzed with the defocused beam.

Regions of melt could be adequately localized on the basis of chemical maps obtained using SEM. In this work, we do not attempt to analyze the incipient melt composition (the smallest Φ). Instead, we cover the most extensive P-T-Φ domain typical of current and primitive upper mantle. As logically expected, the melt composition evolves toward pyrolite, the sample bulk composition, with increasing Φ (Fig. 5). Chemical trends, however, vary significantly with experimental P. Noticeable trends are the following:

1) CaO and Al_2O_3 contents in melt decrease significantly with increasing T because of their known incompatible character. CaO presents a major decrease from 10 to 15 to ~3 wt% at all P, except at 23 to 25 GPa where it becomes slightly less incompatible. Al_2O_3 content also decreases largely with T from ~17 to ~5% at 4 to 5 GPa.

2) The incompatible character of Al disappears with increasing P, as expected from the presence of residual garnet above the solidus for P higher than ~7 GPa. At low Φ, the Al content in the melt increases from ~2 to ~18 wt% with P from 4 to 5 GPa to 23 to 25 GPa, respectively.

3) Our melt FeO contents are low, indicating a moderately incompatible behavior. They present a relative stagnation up to $\Phi \sim 60\%$, independently of the P, except at 23 to 25 GPa. It suggests solid-melt partition coefficients close to unity with the solid phases that disappear before $\Phi \sim 60\%$ and an incompatible behavior only relative to the mineral phase that remain stable up the liquidus. We note that our FeO results diverge from previous works performed at very low melting extents, as significantly higher Fe content is reported in the incipient melt [e.g., (*73*, *74*)].

4) MgO presents a major increase of its content from 15 to 25 wt% to ~40 wt% with increasing Φ. Still, its compatible character decreases with increasing P; its content in the melt at low Φ evolves

from ~15 to ~25 wt% with increasing *P*. At high Φ, melts produced at *P* higher than ~7 GPa contain 25 to 30% MgO, similar to komatiitic liquids.

5) SiO_2 contents in the melt stagnate at 43 to 48 wt% at all Φ and below 23 to 25 GPa. Therefore, upper mantle melts should not be particularly depleted or enriched in SiO_2 compared to pyrolite. The highest melt SiO_2 content is 50 to 52% at 23 to 25 GPa and Φ lower than 20%. This effect can be related to ferropericlase being the liquidus phase in this *P* range [as reported in (*75*) for peridotite].

6) Simultaneous low MgO and stagnant or high SiO_2 contents yield high SiO_2/MgO ratio in the first melts to form [e.g., (*76*)].

7) High Ti, Na, and K concentrations are measured in the first drops of melts (table S4), and these contents decrease fast with increasing Φ, as expected for strongly incompatible elements.

Geodynamical modeling

Following our previous work (*59*), we calculate the time evolution of the pyrolitic-mantle geotherm during the first ~3 Ga of Earth's history. First, we set the primordial mantle *T* gradient parallel and slightly above the mantle solidus. It corresponds to the thermal state of the mushy mantle when the magma ocean has solidified to Φ of ~40% at all depths, several thousand years after the major Moon-forming impact (*77*). We note that this model could rise discussions; still, such highly superadiabatic *T* gradient is very likely to happen after the global magma ocean solidification. Then, we use a one-dimensional numerical model in spherical geometry accounting for turbulent convective heat transfer to calculate the extent of cooling at all mantle depths. This is the same calculations as recently reported for a chondritic-type mantle [see details in (*59*)].

We adopt the physical parameters typical of the pyrolitic mantle model. The composition establishes a number of thermodynamical parameters; e.g., equation of state, heat capacity, and latent heat of fusion, which are all calculated using a mixing model based on the molar fractions of enstatite (37.63%), forsterite (51.64%), fayalite (5.39%), anorthite (3.13%), and diopside (2.22%). Concerning the pyrolite solidus and liquidus, we used (i) the solidus and liquidus measured below ~27 GPa in this study (Fig. 4), (ii) the solidus measured recently in LMV using the laser-heated diamond anvil cell, which is very similar to the solidus of the chondritic-type mantle (*78*), and (iii) the same liquidus as reported for the chondritic-type mantle (*78*) but shifted by −200 K to match the liquidus *T* of pyrolite found at ~25 GPa and ~2500 K in this study.

We observe that the liquidus T profile in the lower mantle does not have a substantial impact on the results of our calculations. When fitted using Simon-Glatzel equations $T_m(P) = T_0(P/a + 1)^{1/c}$, where $T_m(P)$ and P are melting T(K) and P(GPa), respectively, it yields (i) ($T_0 = 1622.7$; $a = 237.79$; $c = 0.33615$) and ($T_0 = 349.82$; $a = 0.10937$; $c = 2.9646$) for the pyrolite solidus at *P* below and above 24 GPa, respectively, and (ii) ($T_0 = 1931.2$; $a = 222.27$; $c = 0.48148$) and ($T_0 = 1498.9$; $a = 10.760$; $c = 2.3668$) for the pyrolite liquidus at *P* below and above 18 GPa, respectively (Fig. 8).

For mantle viscosity, we consider equation 19B of (*59*) with $A_{diff} = 10^{-15}$ Pa^{-1} s^{-1}, $V_{diff} = 10^{-6}$ m^3 mol^{-1}, $E_{diff} = 200$ kJ mol^{-1}, and no dichotomy between upper and lower mantle viscosity. We also considered radiogenic heating as in our previous work.

In addition to the calculated pyrolitic-mantle geotherm as a function of time, we also calculate several mantle adiabatic *T* profiles for the deep mantle. They are primarily constrained by the pyrolite equation of state; however, complications arise at *T* between the solidus and the liquidus, where the degree of mantle partial melting can change with depth. This is taken into account by considering the latent heat of fusion for the variation of Φ with depth, as already described in previous works [e.g., (*50*)]. It yields adiabatic *T* profiles steeper for the mushy mantle between the solidus and liquidus compared to subsolidus mantle conditions (Fig. 8).

SUPPLEMENTARY MATERIALS

Supplementary material for this article is available at https://science.org/doi/10.1126/sciadv.abo1036

REFERENCES AND NOTES

1. C. Herzberg, K. Condie, J. Korenaga, Thermal history of the Earth and its petrological expression. *Earth Planet. Sci. Lett.* **292**, 79–88 (2010).
2. C. Herzberg, M. J. O'Hara, Plume-associated ultramafic magmas of phanerozoic age. *J. Petrol.* **43**, 1857–1883 (2002).
3. C. Herzberg, P. D. Asimow, Petrology of some oceanic island basalts: PRIMELT2.XLS software for primary magma calculation. *Geochem. Geophys. Geosystems* **9**, Q09001 (2008).
4. C.-T. Lee, P. Luffi, T. Plank, H. Dalton, W. Leeman, Constraints on the depths and temperatures of basaltic magma generation on Earth and other terrestrial planets using new thermobarometers for mafic magmas. *Earth Planet. Sci. Lett.* **279**, 20–33 (2009).
5. T. Grove, S. Parman, Thermal evolution of the Earth as recorded by komatiites. *Earth Planet. Sci. Lett.* **219**, 173–187 (2004).
6. I. H. Campbell, R. W. Griffiths, The changing nature of mantle hotspots through time: Implications for the chemical evolution of the mantle. *J. Geol.* **100**, 497–523 (1992).
7. A. Piccolo, B. Kaus, R. White, R. Palin, Generation of earth's early continents from a relatively cool archean mantle. *Geochem. Geophys. Geosystems* **20**, 1679–1697 (2019).
8. S. Matthews, K. Wong, O. Shorttle, M. Edmonds, J. Maclennan, Do olivine crystallization temperatures faithfully record mantle temperature variability? *Geochem. Geophys. Geosystems* **22**, e2020GC009157 (2021).
9. J. Ganne, X. Feng, Primary magmas and mantle temperatures through time. *Geochem. Geophys. Geosystems* **18**, 872–888 (2017).
10. M. Yoshida, A new conceptual model for whole mantle convection and the origin of hotspot plumes. *J. Geodyn.* **78**, 32–41 (2014).
11. R. E. Ernst, *Large Igneous Provinces* (Cambridge University Press, 2014).
12. J. Arndt, S. J. Barnes, C. M. Lesher, *Komatiite* (Cambridge University Press, 2008).
13. J. M. D. Day, Hotspot volcanism and highly siderophile elements. *Chem. Geol.* **341**, 50–74 (2013).
14. S. A. Gibson, Major element heterogeneity in archean to recent mantle plume starting-heads. *Earth Planet. Sci. Lett.* **195**, 59–74 (2002).
15. B. Jahn, G. Gruau, A. Glikson, Komatiites of the Onverwacht Group, S. Africa: REE geochemistry, Sm/Nd age and mantle evolution. *Contrib. to Mineral. Petrol.* **80**, 25–40 (1982).
16. M. le Bas, IUGS reclassification of the high-mg and picritic volcanic rocks. *J. Petrol.* **41**, 1467–1470 (2000).
17. C. Herzberg, M. J. O'Hara, Phase equilibrium constraints on the origin of basalts, picrites, and komatiites. *Earth Sci. Rev.* **44**, 39–79 (1998).
18. D. Green, Genesis of archean peridotitic magmas and constraints on archean geothermal gradients and tectonics. *Geology* **3**, 15–18 (1975).
19. C. Herzberg, J. Zhang, Melting experiments on anhydrous peridotite KLB-1: Compositions of magmas in the upper mantle and transition zone. *J. Geophys. Res.* **101**, 8271–8295 (1996).
20. R. Nomura, K. Hirose, K. Uesugi, Y. Ohishi, A. Tsuchiyama, A. Miyake, Y. Ueno, Low core-mantle boundary temperature inferred from the solidus of pyrolite. *Science* **343**, 522–525 (2014).
21. K. Litasov, E. Ohtani, Phase relations and melt compositions in CMAS–pyrolite–H_2O system up to 25 GPa. *Phys. Earth Planet. Inter.* **134**, 105–127 (2002).
22. T. Inoue, R. P. Rapp, J. Z. Zhang, T. Gasparik, D. J. Weidner, T. Irifune, Garnet fractionation in a hydrous magma ocean and the origin of Al-depleted komatiites: Melting experiments of hydrous pyrolite with REEs at high pressure. *Earth Planet. Sci. Lett.* **177**, 81–87 (2000).
23. M. J. Walter, Melting of garnet peridotite and the origin of komatiite and depleted lithosphere. *J. Petrol.* **39**, 29–60 (1998).
24. M. Boyet, M. Garçon, N. Arndt, R. W. Carlson, Z. Konc, Residual liquid from deep magma ocean crystallization in the source of komatiites from the ICDP drill core in the Barberton Greenstone Belt. *Geochim. Cosmochim. Acta* **304**, 141–159 (2021).
25. C. Herzberg, Generation of plume magmas through time: An experimental perspective. *Chem. Geol.* **126**, 1–16 (1995).

26. A. C. Kerr, G. F. Marriner, N. T. Arndt, J. Tarney, A. Nivia, A. D. Saunders, R. A. Duncan, The petrogenesis of Gorgona komatiites, picrites and basalts: New field, petrographic and geochemical constraints. *Lithos.* **37**, 245–260 (1996).
27. E. Takahashi, Melting of a dry peridotite KLB-1 up to 14 GPa—Implications on the origin of the peridotitic upper mantle. *J. Geophys. Res. Solid Earth Planets* **91**, 9367–9382 (1986).
28. V. Courtillot, A. Davaille, J. Besse, J. Stock, Three distinct types of hotspots in the Earth's mantle. *Earth Planet. Sci. Lett.* **205**, 295–308 (2003).
29. G. Foulger, J. Natland, D. Presnall, D. Anderson, *Plates, Plumes, and Paradigms* (Geological Society of America, 2005).
30. C. A. Dalton, C. H. Langmuir, A. Gale, Geophysical and geochemical evidence for deep temperature variations beneath mid-ocean ridges. *Science* **344**, 80–83 (2014).
31. S. Maruyama, M. Santosh, D. Zhao, Superplume, supercontinent, and post-perovskite: Mantle dynamics and anti-plate tectonics on the core–mantle boundary. *Gondw. Res.* **11**, 7–37 (2007).
32. N. Coltice, H. Bertrand, P. Rey, F. Jourdan, B. R. Phillips, Y. Ricard, Global warming of the mantle beneath continents back to the Archaean. *Gondw. Res.* **15**, 254–266 (2009).
33. L. T. Elkins-Tanton, Continental magmatism, volatile recycling, and a heterogeneous mantle caused by lithospheric gravitational instabilities. *J. Geophys. Res. Solid Earth* **112**, B03405 (2007).
34. C. Hemond, N. T. Arndt, U. Lichtenstein, A. W. Hofmann, N. Oskarsson, S. Steinthorsson, The heterogeneous Iceland plume: Nd-Sr-O isotopes and trace element constraints. *J. Geophys. Res.* **98**, 15833–15850 (1993).
35. F. Jourdan, A. Marzoli, H. Bertrand, S. Cirilli, L. Tanner, D. Kontak, G. McHone, P. Renne, G. Bellieni, ^{40}Ar/^{39}Ar ages of CAMP in North America: Implications for the Triassic–Jurassic boundary and the ^{40}K decay constant bias. *Lithos* **110**, 167–180 (2009).
36. M. G. Jackson, M. D. Kurz, S. R. Hart, R. K. Workman, New Samoan lavas from Ofu Island reveal a hemispherically heterogeneous high 3He/4He mantle. *Earth Planet. Sci. Lett.* **264**, 360–374 (2007).
37. J. Blichert-Toft, N. T. Arndt, Hf isotope compositions of komatiites. *Earth Planet. Sci. Lett.* **171**, 439–451 (1999).
38. T. Matsumoto, A. Seta, J. Matsuda, M. Takebe, Y. Chen, S. Arai, Helium in the Archean komatiites revisited: Significantly high 3He/4He ratios revealed by fractional crushing gas extraction. *Earth Planet. Sci. Lett.* **196**, 213–225 (2002).
39. F. A. Davis, M. M. Hirschmann, M. Humayun, The composition of the incipient partial melt of garnet peridotite at 3 GPa and the origin of OIB. *Earth Planet. Sci. Lett.* **308**, 380–390 (2011).
40. M. B. Baker, E. M. Stolper, Determining the composition of high-pressure mantle melts using diamond aggregates. *Geochim. Cosmochim. Acta* **58**, 2811–2827 (1994).
41. R. J. Kinzler, Melting of mantle peridotite at pressures approaching the spinel to garnet transition: Application to mid-ocean ridge basalt petrogenesis. *J. Geophys. Res. B Solid Earth* **102**, 853–874 (1997).
42. E. Takahashi, T. Shimazaki, Y. Tsuzaki, H. Yoshida, Melting study of a peridotite KLB-1 to 6.5 GPa, and the origin of basaltic magmas. *Philos. Trans. Royal Soc. Phys. Sci. Eng.* **342**, 105–120 (1993).
43. K. Hirose, I. Kushiro, Partial melting of dry peridotite at high-pressures—Determination of compositions of melts segregated from peridotite using aggregates of diamonds. *Earth Planet. Sci. Lett.* **114**, 477–489 (1993).
44. D. Novella, D. J. Frost, The composition of hydrous partial melts of garnet peridotite at 6 GPa: Implications for the origin of group II kimberlites. *J. Petrol.* **55**, 2097–2123 (2014).
45. D. Andrault, G. Pesce, G. Manthilake, J. Monteux, N. Bolfan-Casanova, J. Chantel, D. Novella, N. Guignot, A. King, J.-P. Itie, L. Hennet, Deep and persistent melt layer in the Archaean mantle. *Nat. Geosci.* **11**, 139–143 (2018).
46. R. G. Trønnes, D. J. Frost, Peridotite melting and mineral–Melt partitioning of major and minor elements at 22–24.5 GPa. *Earth Planet. Sci. Lett.* **197**, 117–131 (2002).
47. C. Herzberg, P. Raterron, J. Zhang, New experimental observations on the anhydrous solidus for peridotite KLB-1. *Geochim. Cosmochim. Acta* **1**, 1051-14 (2000).
48. T. Scott, D. L. Kohlstedt, The effect of large melt fraction on the deformation behavior of peridotite. *Geochim. Cosmochim. Acta* **246**, 177–187 (2006).
49. L. Xie, A. Yoneda, D. Yamazaki, G. Manthilake, Y. Higo, Y. Tange, N. Guignot, A. King, M. Scheel, D. Andrault, Formation of bridgmanite-enriched layer at the top lower-mantle during magma ocean solidification. *Nat. Commun.* **11**, 548 (2020).
50. G. H. Miller, E. M. Stolper, T. J. Ahrens, The equation of state of a molten komatiite 2, Application to komatiite petrogenesis and the Hadean mantle. *J. Geophys. Res.* **96**, 11849–11864 (1991).
51. T. Katsura, A. Yoneda, D. Yamazaki, T. Yoshino, E. Ito, Adiabatic temperature profile in the mantle. *Phys. Earth Planet. Inter.* **183**, 212–218 (2010).
52. A. Davaille, A simultaneous generation of hotpots and superswells by convection in a heterogeneous planetary mantle. *Nature* **402**, 756–760 (1999).
53. J. Korenaga, Urey ratio and the structure and evolution of Earth's mantle. *Rev. Geophys.* **46**, RG2007 (2008).
54. K. C. Condie, R. C. Aster, J. van Hunen, A great thermal divergence in the mantle beginning 2.5 Ga: Geochemical constraints from greenstone basalts and komatiites. *Geosci. Front.* **7**, 543–553 (2016).
55. G. F. Davies, Effect of plate bending on the Urey ratio and the thermal evolution of the mantle. *Earth Planet. Sci. Lett.* **287**, 513–518 (2009).
56. H. Iwamori, D. McKenzie, E. Takahashi, Melt generation by isentropic mantle upwelling. *Earth Planet. Sci. Lett.* **134**, 253–266 (1995).
57. C. Herzberg, P. D. Asimow, N. Arndt, Y. Niu, C. M. Lesher, J. G. Fitton, M. J. Cheadle, A. D. Saunders, Temperatures in ambient mantle and plumes: Constraints from basalts, picrites, and komatiites. *Geochem. Geophys. Geosystems* **8**, 2006GC001390 (2007).
58. C. G. Farnetani, A. W. Hofmann, Dynamics and internal structure of the Hawaiian plume. *Earth Planet. Sci. Lett.* **295**, 231–240 (2010).
59. J. Monteux, D. Andrault, M. Guitreau, H. Samuel, S. Demouchy, A mushy Earth's mantle for more than 500 Myr after the magma ocean solidification. *Geophys. J. Int.* **221**, 1165–1181 (2020).
60. N. Arndt, A. Davaille, Episodic earth evolution. *Tectonophysics* **609**, 661–674 (2013).
61. W. B. Moore, A. A. G. Webb, Heat-pipe earth. *Nature* **501**, 501–505 (2013).
62. M. Maurice, N. Tosi, H. Samuel, A. C. Plesa, C. Huttig, D. Breuer, Onset of solid-state mantle convection and mixing during magma ocean solidification. *J. Geophys. Res. Planets* **122**, 577–598 (2017).
63. A. E. Ringwood, in *International Series in the Earth's and Planetary Sciences*, (McGraw-Hill, 1975), pp. 189–194.
64. W. F. McDonough, S. S. Sun, The composition of the earth. *Chem. Geol.* **120**, 223–253 (1995).
65. L. Hennet, V. Cristiglio, J. Kozaily, I. Pozdnyakova, H. E. Fischer, A. Bytchkov, J. W. E. Drewitt, M. Leydier, D. Thiaudiere, S. Gruner, S. Brassamin, D. Zanghi, G. J. Cuello, M. Koza, S. Magazu, G. N. Greaves, D. L. Price, Aerodynamic levitation and laser heating: Applications at synchrotron and neutron sources. *Eur. Phys. J. Spec. Top.* **196**, 151–165 (2011).
66. D. Andrault, M. Muñoz, G. Pesce, V. Cerantola, A. Chumakov, I. Kantor, S. Pascarelli, R. Rüffer, L. Hennet, Large oxygen excess in the primitive mantle could be the source of the great oxygenation event. *Geochem. Perspect. Lett.* **6**, 5–10 (2018).
67. M. Mercier, A. Di Muro, N. Métrich, D. Giordano, O. Belhadj, C. W. Mandeville, Spectroscopic analysis (FTIR, Raman) of water in mafic and intermediate glasses and glass inclusions. *Geochim. Cosmochim. Acta* **74**, 5641–5656 (2010).
68. T. A. Shishkina, R. E. Botcharnikov, F. Holtz, R. R. Almeev, A. M. Jazwa, A. A. Jakubiak, Compositional and pressure effects on the solubility of H_2O and CO_2 in mafic melts. *Chem. Geol.* **388**, 112–129 (2014).
69. A. Boujibar, D. Andrault, M. A. Bouhifd, N. Bolfan-Casanova, J.-L. Devidal, N. Trcera, Metal-silicate partitioning of sulphur, new experimental and thermodynamic constraints on planetary accretion. *Earth Planet. Sci. Lett.* **391**, 42–54 (2014).
70. A. Pommier, K. Leinenweber, D. L. Kohlstedt, C. Qi, E. J. Garnero, S. J. MacKwell, J. A. Tyburczy, Experimental constraints on the electrical anisotropy of the lithosphere-asthenosphere system. *Nature* **522**, 202–206 (2015).
71. Y. Tange, E. Takahashi, Y. Nishihara, K. I. Funakoshi, N. Sata, Phase relations in the system $MgO-FeO-SiO_2$ to 50 GPa and 2000 degrees C: An application of experimental techniques using multianvil apparatus with sintered diamond anvils. *J. Geophys. Res. Solid Earth.* **114**, B02214 (2009).
72. J. Hernlund, K. Leinenweber, D. Locke, J. A. Tyburczy, A numerical model for steady-state temperature distributions in solid-medium high-pressure cell assemblies. *Am. Mineral.* **91**, 295–305 (2006).
73. K. N. Matsukage, Z. Jing, S. I. Karato, Density of hydrous silicate melt at the conditions of Earth's deep upper mantle. *Nature* **438**, 488–491 (2005).
74. P. Condamine, D. J. Frost, in *Annual Report* (Bayerisches Geoinstitute, 2018).
75. E. Ito, A. Kubo, T. Katsura, M. J. Walter, Melting experiments of mantle materials under lower mantle conditions with implications for magma ocean differentiation. *Phys. Earth Planet. Inter.* **143–144**, 397–406 (2004).
76. C. Liebske, D. J. Frost, Melting phase relations in the $MgO-MgSiO_3$ system between 16 and 26 GPa: Implications for melting in Earth's deep interior. *Earth Planet. Sci. Lett.* **345**, 159–170 (2012).
77. J. Monteux, D. Andrault, H. Samuel, On the cooling of a deep terrestrial magma ocean. *Earth Planet. Sci. Lett.* **448**, 140–149 (2016).
78. D. Andrault, N. Bolfan-Casanova, G. Lo Nigro, M. A. Bouhifd, G. Garbarino, M. Mezouar, Melting curve of the deep mantle applied to properties of early magma ocean and actual core-mantle boundary. *Earth Planet. Sci. Lett.* **304**, 251–259 (2011).
79. W. Wang, E. Takahashi, Subsolidus and melting experiments of K-doped peridotite KLB-1 to 27 GPa: Its geophysical and geochemical implications. *Most* **105**, 2855–2868 (2000).
80. H. S. Smith, A. J. Erlank, Geochemistry and petrogenesis of komatiites from the Barberton greenstone belt, South Africa. *Komatiites* , 347–397 (1982).
81. C. Herzberg, Depth and degree of melting of komatiites. *J. Geophys. Res.* **97**, 4521–4540 (1992).
82. Y. Lahaye, N. Arndt, Alteration of a komatiite flow from Alexo, Ontario, Canada. *J. Petrol.* **37**, 1261–1284 (1996).
83. M. J. de Wit, R. A. Hart, R. J. Hart, The Jamestown Ophiolite Complex, Barberton mountain belt: A section through 3.5 Ga oceanic crust. *J. African Earth Sci (1983)* **6**, 681–730 (1987).

84. D. R. Pyke, A. J. Naldrett, O. R. Eckstrand, Archean ultramafic flows in Munro Township, Ontario. *GSA Bull.* **84**, 955–978 (1973).
85. B. Aitken, L. Echeverría, Petrology and geochemistry of komatiites and tholeiites from Gorgona Island, Colombia. *Contrib. to Mineral. Petrol.* **86**, 94–105 (1984).
86. E. Nisbet, N. Arndt, M. Bickle, W. Cameron, C. Chauvel, M. Cheadle, E. Hegner, A. Martin, R. Renner, E. Roedder, Uniquely fresh 2.7 Ga Komatiites from the Belingwe Greenstone-Belt, Zimbabwe. *Geology* **15**, 1147–1150 (1987).
87. M. Bickle, A. Martin, E. G. Nisbet, Basaltic and peridotitic komatiites and stromatolites above a basal unconformity in the Belingwe greenstone belt, Rhodesia. *Earth Planet. Sci. Lett.* **27**, 155–162 (1975).
88. Q. Xie, R. Kerrich, J. Fan, HFSE/REE fractionations recorded in three komatiite-basalt sequences, Archean Abitibi greenstone belt: Implications for multiple plume sources and depths. *Geochim. Cosmochim. Acta* **57**, 4111–4118 (1993).
89. E. Nisbet, M. Bickle, A. Martin, The mafic and ultramafic lavas of the belingwe greenstone belt, Rhodesia. *J. Petrol.* **18**, 521–566 (1977).
90. J. G. Arth, N. T. Arndt, A. J. Naldrett, Genesis of archean komatiites from Munro Township, Ontario: Trace-element evidence. *Geology* **5**, 590–594 (1977).
91. J. A. Hallberg, D. A. C. Williams, Archaean mafic and ultramafic rock associations in the Eastern Goldfields region, Western Australia. *Earth Planet. Sci. Lett.* **15**, 191–200 (1972).
92. S. S. Sun, R. W. Nesbitt, Petrogenesis of Archaean ultrabasic and basic volcanics: Evidence from rare earth elements. *Contrib. to Mineral. Petrol.* **65**, 301–325 (1978).
93. R. Nesbitt, S. S. Sun, A. C. Purvis, Komatiites: Geochemistry and genesis. *Can. Mineral.* **17**, 165–186 (1979).
94. B.-M. Jahn, B. Auvray, S. Blais, R. Capdevila, J. Cornichet, F. Vidal, J. Hameurt, Trace element geochemistry and petrogenesis of finnish greenstone belts. *J. Petrol.* **21**, 201–244 (1980).
95. R. Nesbitt, S.-S. Sun, Geochemistry of Archaean spinifex-textured peridotites and magnesian and low-magnesian tholeiites. *Earth Planet. Sci. Lett.* **31**, 433–453 (1976).
96. D. A. C. Williams, R. G. Furnell, Reassessment of part of the Barberton type area, South Africa. *Precambrian Res.* **9**, 325–347 (1979).
97. G. Gruau, C. Chauvel, N. T. Arndt, J. Cornichet, Aluminum depletion in komatiites and garnet fractionation in the early Archean mantle: Hafnium isotopic constraints. *Geochim. Cosmochim. Acta* **54**, 3095–3101 (1990).
98. T. Chaudhuri, M. Satish-Kumar, R. Mazumder, S. Biswas, Geochemistry and Sm-Nd isotopic characteristics of the Paleoarchean Komatiites from Singhbhum Craton, Eastern India and their implications. *Precambrian Res.* **298**, 385–402 (2017).
99. N. Arndt, Komatiites, kimberlites, and boninites. *J. Geophys. Res.* **108**, 2293 (2003).
100. N. Arndt, A. Fowler, Textures in komatiites and variolitic basalts, in *The Precambrian Earth: Tempos and Events* (Elsevier, 2004).
101. P. A. Sossi, S. M. Eggins, R. W. Nesbitt, O. Nebel, J. M. Hergt, I. H. Campbell, H. S. C. O'Neill, M. Van Kranendonk, D. R. Davies, Petrogenesis and geochemistry of archean komatiites. *J. Petrol.* **57**, 147–184 (2016).
102. Y. Lahaye, N. Arndt, G. Byerly, C. Chauvel, S. Fourcade, G. Gruau, The influence of alteration on the trace-element and Nd isotopic compositions of komatiites. *Chem. Geol.* **126**, 43–64 (1995).
103. S. Sun, (1984).
104. F. F. Guo, S. Svetov, W. D. Maier, E. Hanski, S. H. Yang, Z. Rybnikova, Geochemistry of komatiites and basalts in Archean greenstone belts of Russian Karelia with emphasis on platinum-group elements. *Miner. Depos.* **55**, 971–990 (2020).
105. M. J. Bickle, N. T. Arndt, E. G. Nisbet, J. L. Orpen, A. Martin, R. R. Keays, R. Renner, Geochemistry of the igneous rocks of the Belingwe greenstone belt: Alteration, contamination and petrogenesis, in *The Geology of the Belingwe Greenstone Belt, Zimbabwe* (CRC Press, 2020) pp. 175–213.
106. I. Vlastélic, T. Staudacher, M. Semet, Rapid change of lava composition from 1998 to 2002 at Piton de la Fournaise (Réunion) inferred from Pb isotopes and trace elements: Evidence for variable crustal contamination. *J. Petrol.* **46**, 79–107 (2005).
107. P. M. Holm, R. C. O. Gill, A. K. Pedersen, J. G. Larsen, N. Hald, T. F. D. Nielsen, M. F. Thirlwall, The tertiary picrites of West Greenland: Contributions from 'Icelandic' and other sources. *Earth Planet. Sci. Lett.* **115**, 227–244 (1993).
108. J. F. G. Wilkinson, H. D. Hensel, The petrology of some picrites from Mauna Loa and Kilauea volcanoes, Hawaii. *Contrib. to Mineral. Petrol.* **98**, 326–345 (1988).
109. S. Révillon, N. T. Arndt, E. Hallot, A. C. Kerr, J. Tarney, Petrogenesis of picrites from the Caribbean Plateau and the North Atlantic magmatic province. *Lithos* **49**, 1–21 (1999).
110. A. Kerr, J. Mahoney, Oceanic plateaus: Problematic plumes, potential paradigms. *Chem. Geol.* **241**, 332–353 (2007).
111. A. C. Kerr, *Oceanic Plateaus* (Elsevier, ed. 2, 2014), vol. 4.
112. Z. Zhang, J. J. Mahoney, J. Mao, F. Wang, Geochemistry of picritic and associated basalt flows of the western emeishan flood basalt province, China. *J. Petrol.* **47**, 1997–2019 (2006).
113. D. Wang, S. Karato, Electrical conductivity of talc aggregates at 0.5 GPa: Influence of dehydration. *Phys. Chem. Miner.* **40**, 11–17 (2013).
114. H. Brandstätter, I. Hanzu, M. Wilkening, Myth and reality about the origin of inductive loops in impedance spectra of lithium-ion electrodes—A critical experimental approach. *Electrochim. Acta* **207**, 218–223 (2016).
115. D. Klotz, Negative capacitance or inductive loop?—A general assessment of a common low frequency impedance feature. *Electrochem. Commun.* **98**, 58–62 (2019).
116. T. Yoshino, A. Shimojuku, S. Shan, X. Guo, D. Yamazaki, E. Ito, Y. Higo, K. I. Funakoshi, Effect of temperature, pressure and iron content on the electrical conductivity of olivine and its high-pressure polymorphs. *J. Geophys. Res. Solid Earth* **117**, 1–15 (2012).
117. T. Yoshino, Laboratory electrical conductivity measurement of mantle minerals. *Surv. Geophys.* **31**, 163–206 (2010).
118. J. Zhang, C. Herzberg, Melting experiments on anhydrous peridotite KLB-1 from 5.0 to 22.5 GPa. *J. Geophys. Res.* **99**, 17729–17742 (1994).

Acknowledgments: We thank two anonymous reviewers for their thoughtful comments. We thank L. Hennet for the preparation of the pyrolitic glasses and L. Xie, Q. Dumont, and M. Garçon for help and fruitful discussions. **Funding:** This research was financed by the French Government Laboratory of Excellence initiative no. ANR-10-LABX-0006 and the Université Clermont Auvergne. This is the laboratory of excellence Clervolc contribution no. 561. **Author contributions:** R.P. prepared all experiments. R.P. and G.M. performed the conductivity measurements. R.P., D.A., G.M., N.G., A.K., and L.H. performed the experiments at SOLEIL. R.P. and J.L.D. performed the sample characterization and chemical analyses of melts. J.M. and D.A. elaborated the geodynamic modeling. R.P. and D.A. wrote the manuscript, which was revised by G.M. and J.M. and validated by all coauthors. **Competing interests:** The authors declare that they have no competing interests. **Data and materials availability:** All data needed to evaluate the conclusions in the paper are present in the paper and/or the Supplementary Materials.

Submitted 13 January 2022
Accepted 17 August 2022
Published 2 November 2022
10.1126/sciadv.abo1036

Science Advances

Deep mantle origin of large igneous provinces and komatiites

Rémy PierruDenis AndraultGeeth ManthilakeJulien MonteuxJean Luc DevidalNicolas GuignotAndrew KingLaura Henry

Sci. Adv., 8 (44), eabo1036. • DOI: 10.1126/sciadv.abo1036

Science Advances (ISSN) is published by the American Association for the Advancement of Science. 1200 New York Avenue NW, Washington, DC 20005. The title *Science Advances* is a registered trademark of AAAS.